MMP-2-Activatable Photoacoustic Tumor Imaging Probes Based on Al- and Si-Naphthalocyanines

Koji Miki*, Naoto Imaizumi, Kohei Nogita, Masahiro Oe, Huiying Mu, Wenting Huo, Hiroshi Harada, and Kouichi Ohe*

Corresponding Authors

Koji Miki

Department of Energy and Hydrocarbon Chemistry, Graduate School of Engineering, Kyoto University, Katsura, Nishikyo-ku, Kyoto 615-8510, Japan; orcid/org/0000-0002-4670-2302; Email: kojimiki@scl.kyoto-u.ac.jp

Kouichi Ohe

Department of Energy and Hydrocarbon Chemistry, Graduate School of Engineering, Kyoto University, Katsura, Nishikyo-ku, Kyoto 615-8510, Japan; orcid/org/0000-0001-8893-8893; Email: ohe@scl.kyoto-u.ac.jp

Authors

Naoto Imaizumi, Kohei Nogita, Masahiro Oe, Huiying Mu, Wenting Huo

Department of Energy and Hydrocarbon Chemistry, Graduate School of Engineering, Kyoto University, Katsura, Nishikyo-ku, Kyoto 615-8510, Japan

Hiroshi Harada

Laboratory of Cancer Cell Biology, Graduate School of Biostudies, Kyoto University

Yoshida, Sakyo-ku, Kyoto 606-8501, Japan

Complete contact information is available at: https://pubs.acs.org/0000000000000000.

Author Contributions

K.M. and N.I. conceived and designed the research; N.I. and K.N. executed the synthetic experiments; K.M., N.I., K.N., M.O., H.M., W.H., and H.H. executed the biological experiments; K.O. directed the project and wrote the paper with K.M.

Notes: The authors declare no competing financial interest.

Keywords: photoacoustic, naphthalocyanine, MMP-2, activatable, tumor, imaging

Abstract

Enzyme-activatable photoacoustic probes are powerful contrast agents to visualize diseases in which a specific enzyme is overexpressed. In this study, aluminum and silicon naphthalocyanines (AlNc and SiNc, respectively) conjugated with matrix metalloprotease-2 (MMP-2)-responsive PLGLAG peptide sequence and poly(ethylene glycol) (PEG) as an axial ligand were designed and synthesized. AlNc-peptide-PEG conjugate **AlNc-*pep*-PEG** formed dimeric species interacting with each other through face-to-face *H*-aggregation in water, while SiNc-based conjugate **SiNc-*pep*-PEG** hardly interacted with each other because of the two bulky hydrophilic axial ligands. Both conjugates formed spherical nanometer-sized self-assemblies in water, generating photoacoustic waves under near-infrared photoirradiation. The treatment of MNc-peptide-PEG conjugates (M = Al, Si) with MMP-2 smoothly induced the cleavage of the PLGLAG sequence to release the hydrophilic PEG moiety, resulting in the aggregation of MNcs. By comparing the PA signal intensity changes at 680 nm and 760 nm, the photoacoustic signal intensity ratios were shown to be enhanced by 3–5 times after incubation with MMP-2. We demonstrated that MNc-peptide-PEG conjugates (M = Al, Si) could work as activatable photoacoustic probes in the *in vitro* experiment of MMP-2-overexpressed cell line HT-1080 as well as the *in vivo* photoacoustic imaging of HT-1080-bearing mice.

Introduction

Photoacoustic (PA) imaging is one of the most powerful modalities to visualize disease by utilizing less-invasive near-infrared (NIR) pulse laser irradiation.[1–3] In the visualization of target tissue, disease, and biological activity, PA contrast agents that efficiently absorb photoenergy in the tissue-permeable NIR region

and generate PA waves through nonradiative decay have been intensively investigated.[4,5] To obtain high-contrast PA images, there are three important requirements for PA contrast agents based on organic dyes. First, NIR nonemissive dyes with high molar extinction coefficients are required for strong PA wave generation.[1,6] Second, to assess precisely the pharmacokinetics and therapeutic efficacy of drugs, photostable PA contrast agents that can be tolerated under continuous pulse laser irradiation for repeated diagnosis and biological assessment are preferred.[7–9] Third, to visualize the location of accumulated probes, activatable PA contrast agents that generate PA waves by responding to biological stimuli, especially enzymes, in cells are desired.[10–12] In light of these requirements, the development of activatable PA probes based on a photostable NIR dye is most desirable.

Naphthalocyanine (MNc) is one of the photostable NIR dyes with high ε value (~1×10^5), thereby being expected to be a good candidate as a photosensitizer for PA imaging in the NIR region.[13,14] Despite their blue-shifted absorbance of smaller π-conjugated system, phthalocyanines have widely investigated as a PA contrast agent.[15,16] In contrast, there are a limited number of water-soluble MNcs applying to PA imaging, probably because their low solubility both in organic solvents and water has hampered their functionalization. Lovell and co-workers reported tin naphthalocyanine (SnNc) conjugated with poly(ethylene glycol) (PEG) and its application to PA vascular imaging;[17] however, the "always-on" property of MNcs may preclude their application to PA imaging of target tissues without background noise. Although the "turn-on" property of probes is known to improve the visualization of target tissues dramatically, to our knowledge, there have been no reports involving activatable PA contrast agents based on water-soluble MNcs.

Recently, we reported self-assemblies consisting of NIR dye- and PEG-grafted hyaluronates, in which the aggregated NIR dyes efficiently increased the PA signal intensity in water.[18,19] Based on this finding, we envisioned that the detachment of sterically demanding water-soluble substituents from MNcs would lead to the aggregation of MNcs, resulting in PA signal enhancement (Figure 1). Peripheral aromatics of π-system and axial ligands on a center metal are potential modification sites in MNcs. Although peripheral functionalization is accessible, the aggregation of MNcs cannot be prevented effectively.[20,21] We assumed that conjugation of sterically demanding axial ligands can suppress the aggregation of MNcs, and the removal of axial ligands can

lead to significant PA signal enhancement induced by MNc aggregation. Aiming at detaching the water-soluble ligand in specific cells, we designed MNc-peptide-PEG conjugates consisting of aluminum naphthalocyanine (AlNc) or silicon naphthalocyanine (SiNc), PEG, and a PLGLAG oligopeptide sequence that is cleaved under neutral conditions by matrix metalloprotease-2 (MMP-2) as an overexpressed protease related to tumor metastasis and angiogenesis.[22–24] While photosensitizers of the reported MMP-2-activatable PA contrast agent are NIR cyanine dyes with photobleaching disadvantage,[25–28] no MMP-2-responsive PA contrast agents based on photostable MNcs have been reported. Here, we wish to report newly developed MNc-peptide-PEG conjugates (**MNc-*pep*-PEG**), which smoothly respond to MMP-2, affording MNc aggregates with strong PA wave generation. MMP-2-activatable MNc conjugates were found to increase the relative PA signal intensity ratio up to five times in MMP-2-overexpressed cell line HT-1080 and were successfully applied to *in vivo* PA tumor imaging of HT-1080-bearing mice.

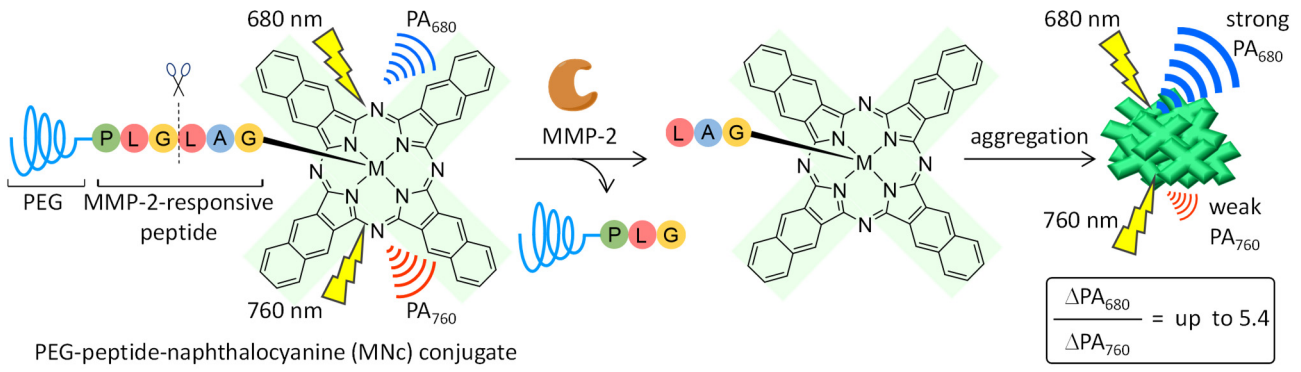

Figure 1. MMP-2-induced MNc-aggregation for PA signal enhancement. AlNc (M = Al) and SiNc (M = Si) were used. In the case of SiNc, two PEG-peptide axial ligands were incorporated on the Si atom, but one of two ligands is omitted for clarity in the figure. P: proline, L: leucine, G: glycine, A: alanine.

Results and Discussion

Synthesis of MNc-*pep*-PEG conjugates (M = Al, Si). For grafting MMP-2-responsive hydrophilic functionality, **AlNc-OH**,[29] which has one hydroxy group as an axial ligand, and **SiNc-OH**,[29] which has two hydroxy groups as axial ligands were chosen as core structures of activatable PA probes (Figure 2). The treatment of **AlNc-OH** and **SiNc-OH** with 3-aminopropylethoxydimethylsilane afforded **AlNc-NH$_2$** and **SiNc-NH$_2$** in moderate yields (Figure S2).[30] **AlNc-*pep*-PEG** and **SiNc-*pep*-PEG** were prepared using a

condensation reaction with peptide-PEG conjugate **2** having a free *C*-terminal, followed by dialysis and lyophilization. The parent signals of **AlNc-*pep*-PEG** and **SiNc-*pep*-PEG** were observed in MALDI-TOF mass spectra (Figure S4). Because the conjugation of PEGs whose average molecular weight was less than 1 kDa led to low water solubility of MNc conjugates, PEG (MW = 2 kDa) as a hydrophilic axial ligand was used. **AlNc-PEG** and **SiNc-PEG** without MMP-2 responsiveness were synthesized by grafting **1** to MNcs in a similar manner (Figure S3).

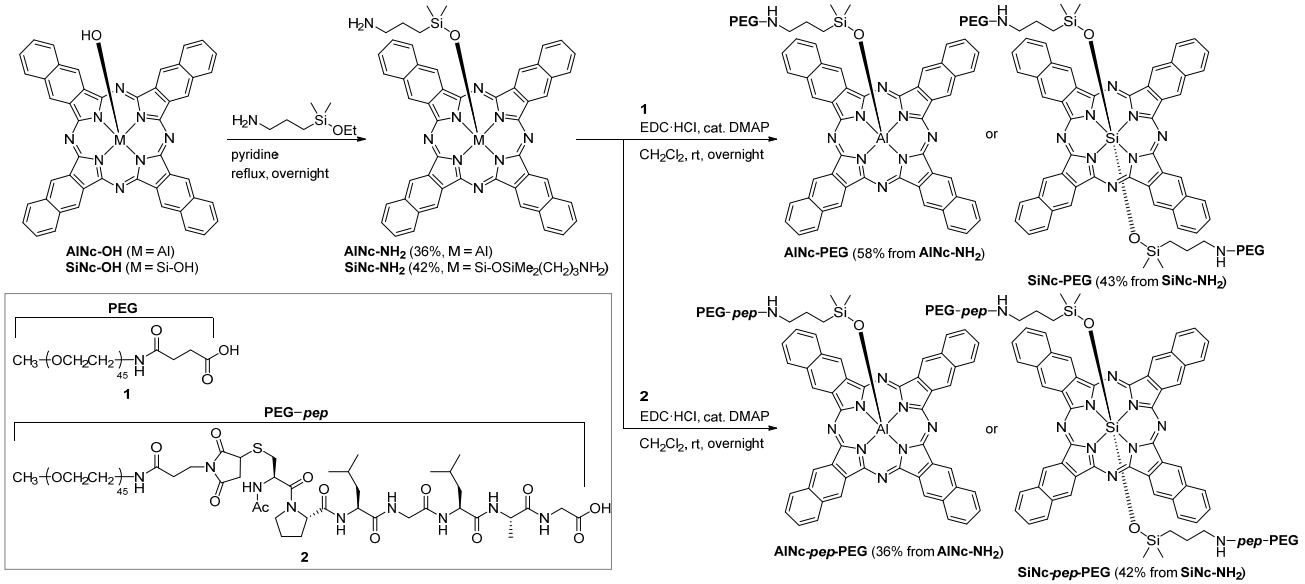

Figure 2. Synthesis of AlNc and SiNc bearing hydrophilic axial ligands. EDC·HCl: 1-ethyl-(3-dimethylaminopropyl)carbodiimide hydrochloride, DMAP: 4-dimethylaminopyridine.

Photophysical properties of MNc-*pep*-PEG conjugates. The absorption maxima of **AlNc-*pep*-PEG** and **SiNc-*pep*-PEG** in *N*,*N*-dimethylformamide (DMF) were detected at 788 nm ($\varepsilon = 1.0 \times 10^5$ M^{-1} cm^{-1}) and 781 nm ($\varepsilon = 1.3 \times 10^5$ M^{-1} cm^{-1}), respectively, which were attributable to the Q-band (orange lines in Figure 3a and 3b).[29] The sharp peak in the NIR region indicates that both conjugates are well dispersed in DMF as a monomeric form without any intermolecular interaction. In contrast, the absorption maximum of **AlNc-*pep*-PEG** in water was observed at 726 nm (blue line in Figure 3a and Table S1). Because the absorbance of MNc *H*-aggregates is known to be observed around 710 nm,[31,32] two **AlNc-*pep*-PEG** molecules are considered to form dimeric face-to-face *H*-aggregates with interaction between their concave faces in water (Figure 4, left).

Nagamura and co-workers reported that pentacoordinated oxovanadium naphthalocyanine (O=VNc) interacted with each other through both *H*-aggregation (λ_{abs} = 745 nm) and *J*-aggregation (λ_{abs} = 850–950 nm).[33] Because no obvious absorption signal of *J*-aggregates of AlNcs was observed, the *J*-aggregation of AlNcs shown in Figure 4 seems to be a minor form probably due to the steric repulsion between the bulky PEG moieties. In the case of **SiNc-*pep*-PEG**, the absorbance of a monomeric form was observed at 789 nm as a sharp signal, although broadened (blue line in Figure 3b and Table S1). This suggests that the interaction of **SiNc-*pep*-PEG** is weak due to the steric bulkiness of the axial ligands (Figure 4, right). **AlNc-PEG** and **SiNc-PEG** showed quite similar absorption spectra to **AlNc-*pep*-PEG** and **SiNc-*pep*-PEG**, respectively, indicating that an MMP-2-responsive peptide does not interact intermolecularly through hydrogen bonds (Figure S5 and Table S1).

Dynamic light scattering (DLS) measurements suggest that **AlNc-*pep*-PEG** and **SiNc-*pep*-PEG** self-assembled to form nanoparticles with diameters of 121 ± 26 and 66 ± 17 nm, respectively (Figure 3c and 3d). From transmission electron microscope (TEM) measurements, small spherical nanoparticles (diameter = 6–7 nm) and slightly larger nanoparticles (diameter = 25–32 nm) were observed in both cases, which might be a mixture of micelles and multimicellar aggregates (Figure S6 and Table S2). We measured the PA waves of **AlNc-*pep*-PEG** and **SiNc-*pep*-PEG** self-assemblies in water to investigate the effect of MNc aggregation on PA signal intensity (Figure 3e and 3f). Under photoirradiation with a pulse laser at 760 nm, PA signal intensity (denoted as PA_{760}) of **SiNc-*pep*-PEG** was 2.6 times stronger than PA_{760} of **AlNc-*pep*-PEG**. The two axial ligands of monomeric **SiNc-*pep*-PEG** might convert the excited photoenergy more efficiently through a nonradiative deactivation pathway, thereby generating stronger PA waves. By contrast, the PA_{680} of **AlNc-*pep*-PEG** and **SiNc-*pep*-PEG** under photoirradiation at 680 nm were comparable (**AlNc-*pep*-PEG** : **SiNc-*pep*-PEG** = 1 : 0.96). By considering that the photoenergy at 680 nm is mainly absorbed by AlNc *H*-aggregates, we reasoned that PA waves can be generated by dye aggregation. To check the influence of pH, we measured PA signal intensities of probes under neutral and slightly acidic conditions. We confirmed that PA signal intensities PA_{680} and PA_{760} as well as the ratios of PA_{680}/PA_{760} are almost constant in pH range from 5.0 to 7.7 (Figure S7).

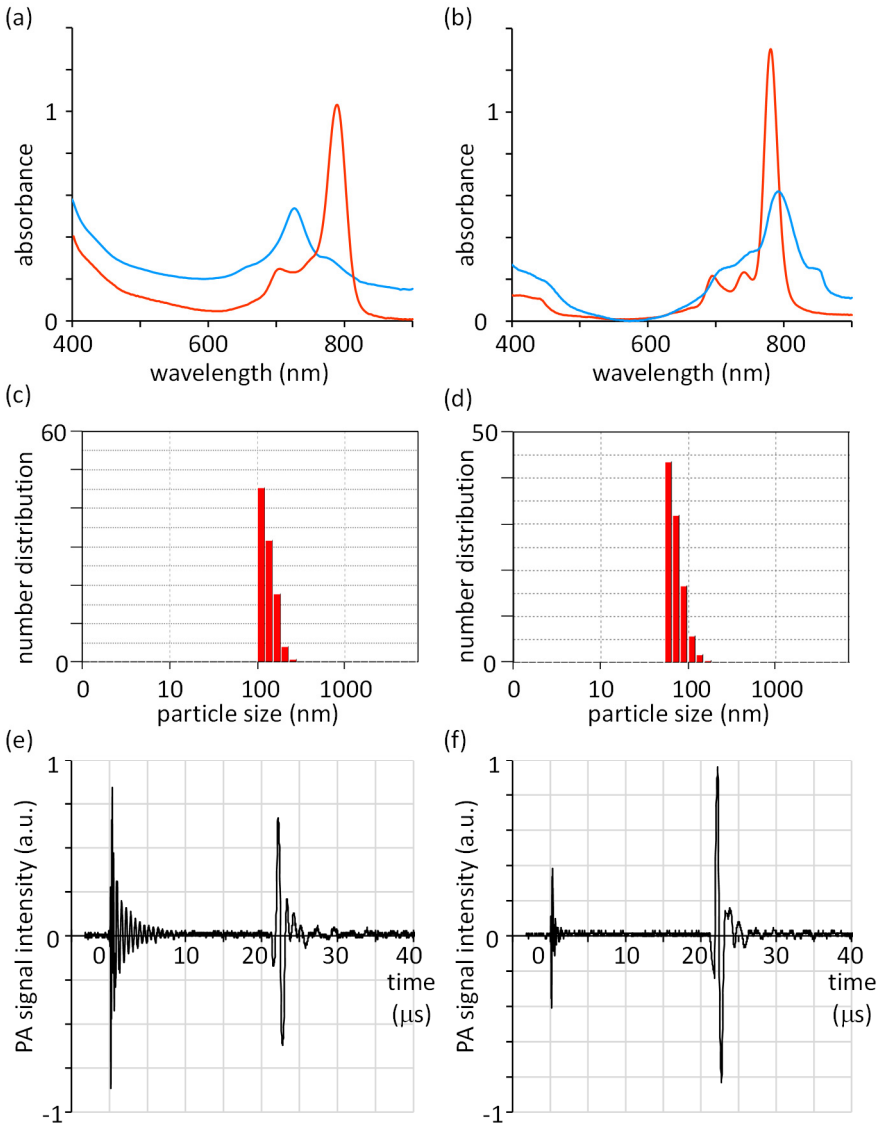

Figure 3. UV-vis absorption spectra of (a) **AlNc-*pep*-PEG** and (b) **SiNc-*pep*-PEG** in DMF (orange) and H_2O (blue). Concentration: 10 μM. Hydrodynamic diameters of self-assemblies consisting of (c) **AlNc-*pep*-PEG** and (d) **SiNc-*pep*-PEG** in H_2O measured by DLS. PA signal of (e) **AlNc-*pep*-PEG** and (f) **SiNc-*pep*-PEG** in H_2O (at 760 nm). Signals were detected at ca. 20 μs after detection of a trigger signal.

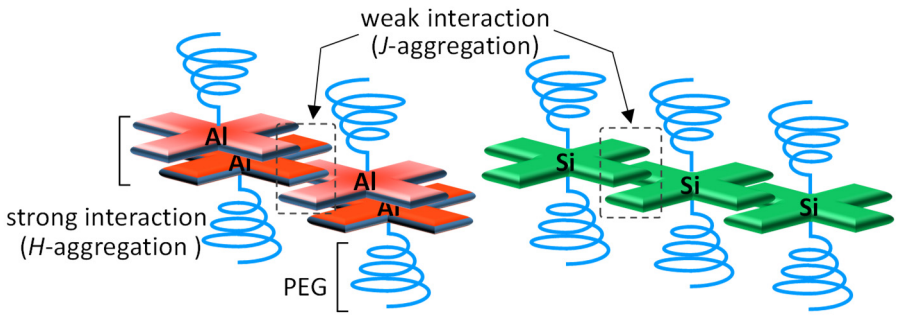

Figure 4. Plausible aggregation modes (*H*- and *J*-aggregates) of **AlNc-*pep*-PEG** (left) and **SiNc-*pep*-PEG** (right).

The photostability under NIR photoirradiation was examined by monitoring the time-dependent decrease in the maximum absorbance (Figure 5). Seventy percent of indocyanine green (ICG),[34,35] which is an approved contrast agent for NIR optical imaging under photoirradiation was bleached after photoirradiation for 2 h, whereas no absorbance decrease of **AlNc-*pep*-PEG** was observed. This property is advantageous for PA imaging under continuous photoirradiation and preparable to lower the limit of detection. **SiNc-*pep*-PEG** was found to be less stable than **AlNc-*pep*-PEG** and 15% of them underwent bleaching after 2 h photoirradiation. Because the photoinduced cleavage of the axial ligand from silicon phthalocyanine has been reported,[30] a similar removal of axial ligands is assumed to proceed to form aggregates, resulting in the absorbance decrease.

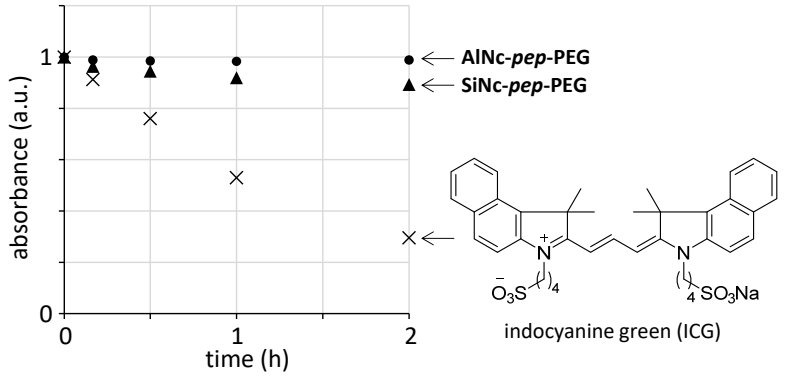

Figure 5. Photobleaching test of **AlNc-*pep*-PEG** (circle), **SiNc-*pep*-PEG** (triangle), and indocyanine green (cross) under LED photoirradiation. LED: λ_{max} = 737 nm, half-bandwidth = 20 nm, power = 25 mW (at the sample level). Absorbance corresponds to the mean value of two independent experiments.

MMP-2 responsiveness of MNc-peptide-PEG conjugates. With photostable MNc conjugates in hand, we next examined their MMP-2 responsiveness. Treating MNc conjugates with MMP-2, the time-dependent change of absorbance was monitored (Figures 6a–c). After 2 h incubation with MMP-2, **AlNc-PEG**, which does not contain MMP-2-responsive peptide, showed no change of absorption spectra. The treatment of **AlNc-*pep*-PEG** and **SiNc-*pep*-PEG** with MMP-2 led to a decrease in absorbance intensity without obvious spectrum shape change. After 2 h incubation, the hydrodynamic diameters of self-assemblies in solution increased in both cases (Figure S8 and Table S3). These results indicate that MMP-2 gradually hydrolyzed the peptide sequence, inducing the aggregation of MNcs. To investigate the aggregation-induced PA signal enhancement,

PA signal intensities were measured before and after incubation of **AlNc-*pep*-PEG** and **SiNc-*pep*-PEG** with MMP-2 for 2 h. By dividing PA signal intensity measured after incubation by that before incubation, the PA signal intensity change (denoted as ΔPA) was calculated. ΔPA_{680} of **AlNc-*pep*-PEG** and **SiNc-*pep*-PEG** increased to 2.0 and 2.5 after incubation for 2 h, respectively, whereas ΔPA_{760} decreased to 0.7 and 0.6, respectively (Figures 6d and 6e, Table 1). Accordingly, both AlNc- and SiNc-conjugates were found to act as activatable probes for MMP-2 detection by monitoring PA_{680}. By focusing on the increase in ΔPA_{680} and the decrease in ΔPA_{760} after incubation, we assumed that the relative PA signal intensity ratio $\Delta PA_{680}/\Delta PA_{760}$ could more clearly track the MMP-2 activity. Indeed, the ratios $\Delta PA_{680}/\Delta PA_{760}$ were 3.1 for **AlNc-*pep*-PEG** and 4.7 for **SiNc-*pep*-PEG** after incubation for 2 h (Table 1), supporting that the change in $\Delta PA_{680}/\Delta PA_{760}$ is more accurate for MMP-2 detection than that in ΔPA_{680}. To evaluate the enzyme specificity, **AlNc-*pep*-PEG** and **SiNc-*pep*-PEG** were treated with other enzymes including other MMPs and MMP-2 in the presence of its inhibitor GM6001 (Figures 6d and 6e).[36] The $\Delta PA_{680}/\Delta PA_{760}$ of **AlNc-*pep*-PEG** and **SiNc-*pep*-PEG** did not significantly change, indicating the MMP-2-specific response of the probes. PA signal intensities PA_{680} and PA_{760} were affected by the concentration of MMP-2 loaded (Figure 6f and Figure S10). At low concentration of MMP-2 (<5 μM), PA_{680} after 2 h incubation linearly increased as the concentration increased. In contrast, PA_{760} decreased linearly, therefore, the ratio $\Delta PA_{680}/\Delta PA_{760}$ gradually increased (Figure 6g). PA signal intensities reached to a plateau when the initial concentration of MMP-2 was more than 5 μM, indicating that both probes are potentially applicable as a "turn-on"-type ratiometric probe for MMP-2 activity at low concentration. To examine the concentration dependence of the enzymatic reaction, enzymatic kinetic parameters (Michaelis constant K_m, turnover number k_{cat}, and k_{cat}/K_m) of MMP-2 hydrolysis of MNc-peptide-PEG conjugates were measured according to Michaelis-Menten analysis (Figure S9 and Table S4). Those parameters for hydrolysis of both **AlNc-*pep*-PEG** (K_m = 22 μM and k_{cat} = 0.0023 s^{-1}, $k_{cat}/K_m = 2.5 \times 10^4$ M^{-1} s^{-1}) and **SiNc-*pep*-PEG** (K_m = 27 μM and k_{cat} = 0.0033 s^{-1}, $k_{cat}/K_m = 3.0 \times 10^4$ M^{-1} s^{-1}) were obtained. Because the kinetic parameters are comparable to those of the reported MMP-2-responsive optical probes,[37–39] the enzyme approach to the peptide moiety was found to be not blocked by the bulky PEG group and MNc moiety.

Because the MMP-2 responsiveness of probes utilizing the PA signal output was proven, we next evaluated

the *in vitro* sensing ability of probes in MMP-2-overexpressed human sarcoma cell line HT-1080.[28,40] Before cell experiments, we confirmed the low cytotoxicity of probes using an MTT assay (Figure S11). After the treatment of HT-1080 with **AlNc-*pep*-PEG** and **SiNc-*pep*-PEG** for 4 h, ΔPA_{680} gradually increased to 4.3 and 2.6, respectively (Figure 6f). Moreover, the values of $\Delta PA_{680}/\Delta PA_{760}$ after 4 h were 5.4 for **AlNc-*pep*-PEG** and 3.9 for **SiNc-*pep*-PEG** (Figure 6g). The incubation with inhibitor GM6001 efficiently suppressed the MMP-2 activity in cells, the PA signal intensities remaining unchanged. The treatment of probes with human cervical cancer cell line HeLa, which is characterized with low MMP-2 expression level,[39] showed a negligible change in PA signal intensities. These results demonstrate that **AlNc-*pep*-PEG** and **SiNc-*pep*-PEG** can work as activatable probes for MMP-2 activity in a living system.

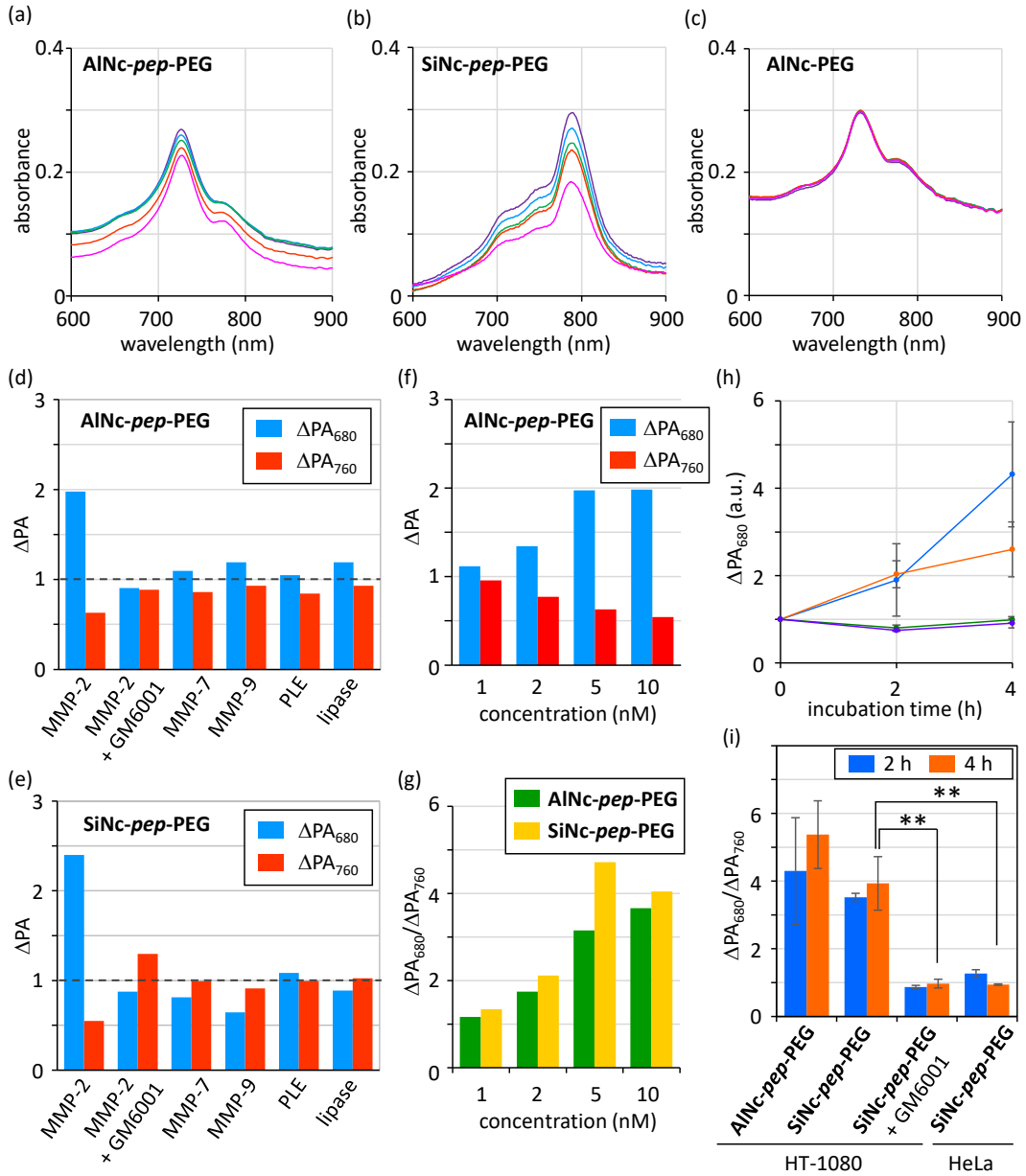

Figure 6. Time-dependent absorbance change of (a) **AlNc-*pep*-PEG**, (b) **SiNc-*pep*-PEG**, and (c) **AlNc-PEG** (5.0 μM, pH = 7.2) during incubation with MMP-2 (5.0 nM). Just after (purple), 15 min (blue), 30 min (green), 60 min (red), and 120 min (pink). PA signal intensity change (ΔPA) of (d) **AlNc-*pep*-PEG** and (e) **SiNc-*pep*-PEG** (30 μM, pH = 7.2) after incubation with enzyme (0.32 μg/mL) for 2 h. Values correspond to the mean value of two independent experiments. PLE: porcine liver esterase, lipase: lipase AK Amano. GM6001: inhibitor of MMP-2. (f) PA signal intensity change (ΔPA) of **AlNc-*pep*-PEG** and (g) ratio of PA intensity change ($\Delta PA_{680}/\Delta PA_{760}$) of **AlNc-*pep*-PEG** and **SiNc-*pep*-PEG** (30 μM, pH = 7.2) after incubation with MMP-2 for 2 h. (h) PA signal intensity change at 680 nm (ΔPA_{680}) during the incubation of HT-1080 with **AlNc-*pep*-PEG** (blue), **SiNc-*pep*-PEG** (orange), **SiNc-*pep*-PEG** and GM6001 (green), and the incubation of HeLa with **SiNc-*pep*-PEG** (purple). Dyes (30 μM) and GM6001 (100 μM). (i) Ratio of PA intensity change ($\Delta PA_{680}/\Delta PA_{760}$) under the same incubation conditions shown in (h). Averages and standard deviations (n = 3) for cell experiments are shown. Two-tailed Student's *t*-test: $^{**}P<0.05$.

Table 1. PA intensity ratios ΔPA_{680}, ΔPA_{760}, and $\Delta PA_{680}/\Delta PA_{760}$.

MNc conjugate		MMP-2	MMP-2 with inhibitor[a]	MMP-9	MMP-7	PLE[b]	lipase[c]
AlNc-*pep*-PEG	ΔPA_{680}	2.0	0.9	1.1	1.2	1.0	1.2
	ΔPA_{760}	0.6	0.9	0.9	0.9	0.8	0.9
	$\Delta PA_{680}/\Delta PA_{760}$	3.1	1.0	1.3	1.3	1.2	1.3
SiNc-*pep*-PEG	ΔPA_{680}	2.5	0.9	0.8	0.6	1.1	0.9
	ΔPA_{760}	0.5	1.3	1.0	0.9	1.0	1.0
	$\Delta PA_{680}/\Delta PA_{760}$	4.7	0.7	0.8	0.7	1.1	0.9

Enzymes (5 nM) were treated with probes (30 μM) in buffered solution (pH = 7.2) at 37 °C for 2 h. [a]GM6001 (inhibitor, 100 μM). [b]Porcine liver esterase. [c]Lipase AK Amano.

***In vivo* PA imaging**. To verify the MMP-2-responsive enhancement of PA signal intensity *in vivo*, we then carried out *in vivo* PA imaging experiments using nude mice bearing HT-1080 in the right leg. Because **AlNc-*pep*-PEG** showed a slightly better $\Delta PA_{680}/\Delta PA_{760}$ value than **SiNc-*pep*-PEG** in the cell experiments, we selected **AlNc-*pep*-PEG** for *in vivo* PA imaging experiments. After intravenous (*i.v.*) injection of **AlNc-*pep*-PEG** or **AlNc-PEG** as a control contrast agent, PA images were obtained under photoirradiation at 680 nm and 760 nm (Figures 7a, 7b and Figure S12). To reduce the effect of background PA signal intensities mainly generated from hemoglobin, the PA signal intensity at 850 nm was subtracted from those at 680 nm and 760 nm and PA signal intensities $PA_{680,vivo}$ and $PA_{760,vivo}$ of probes at the tumor site were estimated. In the case of **AlNc-PEG**, both $PA_{680,vivo}$ and $PA_{760,vivo}$ slightly increased as the probe accumulated through the enhanced permeation and retention effect.[41] The PA signal intensity ratios ($PA_{680,vivo}/PA_{760,vivo}$) of **AlNc-PEG** at 1 h and 6 h after administration were 1.8 ± 0.4 and 1.9 ± 0.3, respectively (Figure 7c and Table S5). Because these $PA_{680,vivo}/PA_{760,vivo}$ values are comparable to the PA signal intensity ratio (PA_{680}/PA_{760} = 1.3) of **AlNc-PEG** in water, **AlNc-PEG** was hardly decomposed in the MMP-2-overexpressed tumor site. On the other hand, the ratio of $PA_{680,vivo}/PA_{760,vivo}$ for **AlNc-**

***pep*-PEG** increased to be 2.5 ± 0.1 as early as 1 h after administration and was retained until 6 h after administration ($PA_{680,vivo}/PA_{760,vivo}$ = 2.5 ± 0.2). These results clearly indicate that PA imaging using **AlNc-*pep*-PEG** can visualize the MMP-2-overexpressed tumor site more clearly than probes without MMP-2 responsiveness. In addition, by considering that the cumulative photoirradiation for 18 min (3 min irradiation at each wavelength) did not lead to the significant decrement of PA signal intensities, **AlNc-*pep*-PEG** and **SiNc-*pep*-PEG** are good candidates for repeated imaging or diagnosis under continuous photoirradiation *in vivo*.

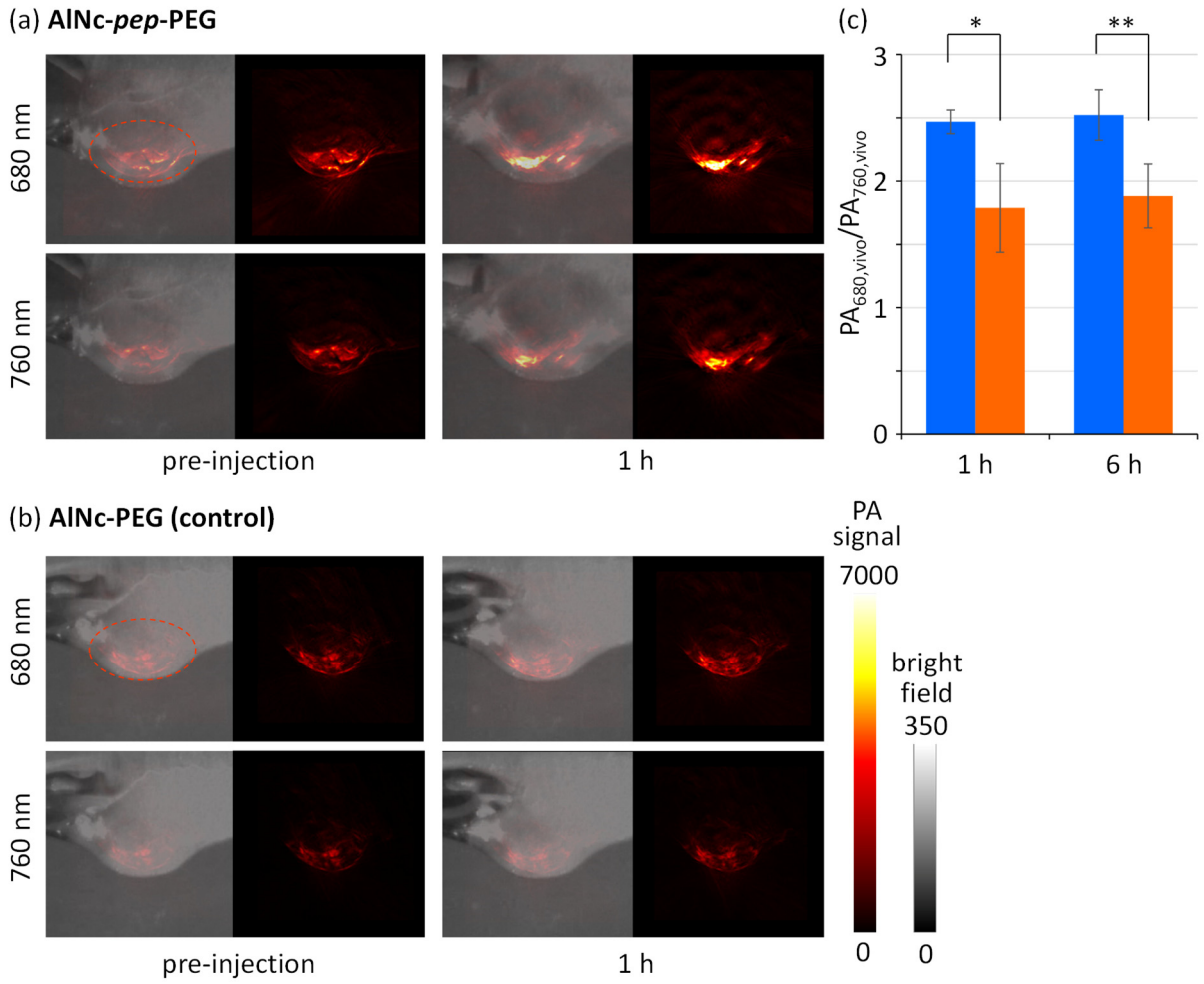

Figure 7. Representative *in vivo* PA images (tumor site) of HT-1080-bearing mice before and 1 h after *i.v.* injection of (a) **AlNc-*pep*-PEG** and (b) **AlPc-PEG** (100 μM in saline, dose: 200 μL). PA signal image (right) and merged image of PA signal image with bright field image (left). Red dotted circle: tumor site. Photoirradiation wavelength: 680 nm and 760 nm. (c) PA signal intensity ratio ($PA_{680,vivo}/PA_{760,vivo}$) at the tumor site of HT-1080-bearing mice 1 h and 6 h after *i.v.* injection of **AlNc-*pep*-PEG** (blue) and **AlNc-PEG** (orange). Averages and standard deviations (n = 3) are shown. Two-tailed Student's *t*-test: *p<0.1, **p<0.05.

Conclusion

We have developed the first example of an enzyme-activatable PA probe based on AlNc and SiNc. AlNc-peptide-PEG conjugate **AlNc-*pep*-PEG** forms *H*-aggregates through π–π interaction between their concave faces, whereas SiNc-based conjugate **SiNc-*pep*-PEG** shows weak intermolecular interaction even in water. After the treatment of probes with MMP-2, the aggregation of the resulting MNc fragments led to an increase in PA_{680}, whereas a decrease in PA_{760} was observed. Kinetic experiments supported that both **AlNc-*pep*-PEG** and **SiNc-*pep*-PEG** respond smoothly to MMP-2. By monitoring the ratio of $\Delta PA_{680}/\Delta PA_{760}$, the MMP-2-specific response of probes was confirmed through both enzymatic reactions and *in vitro* cell experiments. Furthermore, at low concentration of MMP-2 (<5 μM), we confirmed that **AlNc-*pep*-PEG** and **SiNc-*pep*-PEG** are applicable as potential "turn-on"-type ratiometric probes for MMP-2 activity. In *in vivo* PA imaging experiments, we confirmed that the MMP-2-activatable probe **AlNc-*pep*-PEG** successfully visualized the MMP-2-overexpressed tumor tissues. By assuming their activatable property as well as photostability, MNc-peptide-PEG conjugates will be applicable as PA contrast agents for diagnosis and pharmacokinetic evaluation under continuous photoirradiation.

Experimental Section

Materials and Methods. (3-Aminopropyl)dimethylethoxysilane, 4-dimethylaminopyridine (DMAP), copper sulfate, dichloromethane (CH_2Cl_2), pyridine, *N*,*N*-dimethylformamide (DMF) Dulbecco's modified Eagle's medium (DMEM), Eagle's minimum essential medium (EMEM), fetal bovine serum (FBS), and 1% penicillin/streptomycin (P/S) were purchased from Fujifilm-Wako Pure Chemicals Industries, Ltd. (Japan). Indocyanine green (ICG) and (3-(4,5-dimethylthazol-2-yl)-2,5-diphenyltetrazolium bromide (MTT) were purchased from Tokyo Chemical Industry Co., Ltd. (Japan). 1-Ethyl-(3-dimethylaminopropyl)carbodiimide hydrochloride (EDC·HCl) was purchased from Watanabe Chemical Industries, Ltd. (Japan). Sodium chloride (NaCl), dimethylsulfoxide (DMSO), and phosphate buffered saline (PBS) were purchased from nacalai tesque (Japan). Dialysis membrane, Spectra/Por 6 (molecular weight cutoff (MWCO): 3.5K and 25K) was purchased from Spectrum Laboratories Inc. (Rancho Dominguez, CA, USA). Before use, pyridine was distilled over

CaH_2. Other reagents and solvents were used as received. **AcNc-OH** and **SiNc-OH** were prepared according to the reported methods.[29]

UV-vis absorption spectra were recorded by UH5300, Hitachi High Technologies, Japan. Mass spectra were measured by Ultraflex III (MALDI-TOF, Bruker Co., USA). Dynamic light scattering was measured by FPAR-1000 (Otsuka Electronics Co., Ltd., Japan). At least 3 h before measurement, the sample solutions were diluted in water (Milli-Q, 200 μM) and filtered (syringe filter, 0.45 μm pore size, PVDF). The measurements were performed at scattering angles of 90° at 25 °C and the number distribution was summarized.

Photoacoustic (PA) signals of samples in water (Milli-Q, concentration: 3.0×10^{-5} M (dye)) or cell suspension were measured in borosilicate glass cuvette (volume: ca. 200 μL, length: 1 mm, width: 10 mm) by in-house built PA signal measurement apparatus according to the reported procedure.[19] By irradiating a sample solution with pulse laser light, the ultrasonic waves generated from the sample was detected with a piezoelectric element. The PA signal intensity was determined by amplifying the detected signal with a high-speed preamplifier, followed by acquiring the amplified signal with a digital oscilloscope. A pulse laser (nitrogen laser (GL-3300)-dye laser (GL-301), Photon Technology International, USA, 3-ethyl-2-[7-(3-ethyl-2(3H)-benzoxazolylidene)-1,3,5-heptatrienyl]benzoxazolium iodide (DOTC) for 760 nm and oxazine 170 perchlorate for 680 nm) as a light source, an ultrasonic transducer (Panametrics-NDT V303, Olympus, Japan), an ultrasonic preamplifier (Model 5682, Olympus, Japan), and digital phosphor oscilloscopes (DPO4104, Tektronix, USA) were used for measurement. The measurement conditions are as follows: trigger, detection of PA signal with a photodiode; data acquisition, 128 times (128 pulses). For measurement of dye solutions, the effect of absorbance difference was eliminated by normalizing the PA signal intensity by the absorbance of MNcs and the power of pulse laser.

Synthesis of AlNc-NH_2 and SiNc-NH_2. In 200 mL flame-dried two-necked round-bottom flask, a solution of **AlNc-OH** (30 mg, 40 μmol) and (3-aminopropyl)dimethylethoxysilane (38 μL, 0.20 mmol) in pyridine (100 mL) was refluxed under N_2 atmosphere overnight. After removal of solvent under reduced pressure, the residue was dissolved in small amount of CH_2Cl_2. The organic layer was washed with $CuSO_4$ aqueous solution

(5 mL) and dried over $MgSO_4$. After removal of solvent under reduced pressure, **AlNc-NH$_2$** (crude product, 12 mg, ~36%) was obtained as a green solid. Further transformation was carried out without purification, because **AlNc-NH$_2$** stored in a freezer gradually decomposed and aggregated to form insoluble materials. Signals were not observed in NMR measurements due to aggregation. The parent peak of **AlNc-NH$_2$** was observed by MALDI-TOF mass spectroscopy (matrix: 2,5-dihydroxybenzoic acid (DHB)), together with inseparable dimeric byproduct (Figure S2). **SiNc-NH$_2$** was prepared by the similar synthetic method for **SiNc-OH** (~42% yield, a green solid) and used for further transformation without purification. The parent signal of **SiNc-NH$_2$** was not detected in MALDI-TOF mass spectrum, and signals were not observed in NMR measurements due to aggregation. Because of their low solubility in common organic solvents, UV-vis absorption spectra were not measured.

Synthesis of AlNc-PEG, SiNc-PEG, AlNc-*pep*-PEG, and SiNc-*pep*-PEG. In 50 mL flame-dried two-necked round-bottom flask, dry CH_2Cl_2 (5 mL), compound **1**[42] (23 mg, 11 μmol), EDC·HCl (9 mg, 44 μmol), a solution of DMAP (0.3 mg, 2.5 μmol) in CH_2Cl_2 (100 μL) were successively added and the resulting mixture was stirred at room temperature for 1 h. To this solution was added **AlNc-NH$_2$** (10 mg, 11 μmol) and the resulting mixture was stirred at room temperature overnight. The organic solvent was removed under reduced pressure and the residue was dissolved in water (5 mL). The suspension was centrifuged and the supernatant was dialyzed against water for 1 day by using Spectra/Por 6 (MWCO = 25K). **AlNc-PEG** (15 mg, 5.1 μmol, 46%) was obtained as a green solid after lyophilization. **SiNc-PEG** (51% yield, a green solid) was prepared from **SiNc-NH$_2$** by the similar synthetic method for **AlNc-PEG**. **AlNc-*pep*-PEG** and **SiNc-*pep*-PEG** were obtained as a green solid in 58% and 43% yields, respectively, by the similar synthetic method for **AlNc-PEG** and **SiNc-PEG**, in which compound **2** (see the Supporting Information) was used instead of **1**. The parent signals of MNc-PEG conjugates and MNc-peptide-PEG conjugates (M = Al, Si) were detected by MALDI-TOF mass spectrometry (Figure S3 and S4). Although PEG signals detected in ^{1}H NMR were strong, the signals of MNc skeleton were not observed in $CDCl_3$, d_6-DMSO, and D_2O, probably because of their amphiphilicity and aggregation (see the Supporting Information).

Photostability of AlNc-*pep*-PEG and SiNc-*pep*-PEG. **AlNc-*pep*-PEG**, **SiNc-*pep*-PEG**, and ICG were dissolved in phosphate buffer solution (pH = 7.2, 3 mL, 15 μM). To minimize the influence of the background signal, the absorbance of all solutions was adjusted to approximately 1.0. All solutions were transferred into quartz cells and irradiated using a LED photoirradiation apparatus (CL-1501, Asahi Spectra Co., Ltd., Japan) equipped with LED head unit (CL-H1-730-9-1, λ_{max} = 737 nm, half-bandwidth = 20 nm, power = 25 mW at the sample level). The time-dependent photobleaching was monitored by measuring the absorbance at the maximum.

Enzyme responsiveness. Recombinant human MMP-2 (3 μL, 5.0 μM, PeproTech Inc., USA) in Milli-Q was added to a solution of dyes (5.0 μM, 3 mL) in PBS (pH = 7.2) and the resulting mixture ([MMP-2] = 5.0 nM) was incubated at 37 °C. The enzymatic reaction was monitored by measurement of absorbance. For evaluation of enzyme-specificity of dyes, dyes (30 μM, 3 mL) in PBS (pH = 7.2) were incubated with enzyme (3 μL, 5.0 μM) at 37 °C. Before and after 2 h incubation, PA signal intensities were measured at 680 nm and 760 nm Recombinant human MMP-7 (BioLegend Inc., USA), MMP-9 (RayBiotech Inc., USA), PLE (porcine liver esterase, Roche, Switzerland), lipase AK Amano (Fujifilm-Wako Pure Chemicals Industries, Ltd., Japan), and GM6001 (inhibitor, 100 μM, Cayman Chemical, USA) were used. Evaluation of enzyme kinetics is found in the Supporting Information.

Cell culture. Human cervical epithelial adenocarcinoma cell line (HeLa) and Human sarcoma cell line (HT-1080) were purchased from American Type Culture Collection and National Institutes of Biomedical Innovation, Health and Nutrition, respectively. HeLa and HT-1080 cells were cultured in DMEM and EMEM supplemented with 10% FBS and 1% P/S, respectively. The cells were cultured well-humidified incubator with 5% CO_2 and 95% air at 37 °C.

Cell experiment. HeLa and HT-1080 cells were seeded into 12-well plate at a density of 5×10^4 cells/well.

The cells were incubated at 37 °C for 24 h for cell attachment, and incubated with dyes (30 μM, 1 mL) in DMEM (for HeLa) and EMEM (for HT-1080) with 10% FBS and 1% P/S at 37 °C for 2 h or 4 h. After incubation, cells were washed with PBS twice and detached by cell scraper. The cell suspension in PBS was poured into borosilicate glass cuvette and measured by in-house built PA signal measurement apparatus. For inhibition experiment, cells were incubated with **Si-*pep*-PEG** (30 μM) and GM6001 (100 μM).

***In vivo* PA imaging** Female BALB/c mice in 6–9 weeks of age were purchased from Japan SLC, Inc., Japan. The mice were housed at the Institute of Laboratory Animals at Graduate School of Medicine of Kyoto University. All of our animal experiments were approved by the Animal Research Committee of Kyoto University and carried out with its guidelines.

Female BALB/c mice were chosen to prepare the tumor-bearing mice by injection of HT-1080 cells ($1.0–1.3 \times 10^6$ cells) in the right leg of each mouse. The tumor size was carefully monitored in the Radiation Biology Center, Kyoto University. The tumor-bearing mice were treated with **AlNc-*pep*-PEG** and **AlNc-PEG** (100 μM in 200 μL saline) through *i.v.* injection. *In vivo* PA imaging was performed on Nexus 128 scanner manufactured by Endra Life Sciences (Ann Arbor, MI, USA). PA images were obtained under photoirradiation at 680 nm, 760 nm, and 850 nm (3 min continuous pulse laser irradiation, 9 min irradiation in total) at indicated time points. The PA intensities at 680 nm, 760 nm, and 850 nm in the region of interest (ellipse shape, 10 mm×14 mm axes) were calculated by OsiriX according to the instruction. To omit the effect of PA signal from hemoglobin, we calculated the PA signal intensities $PA_{680,vivo}$ at 680 nm and $PA_{760,vivo}$ at 760 nm by the subtraction of PA signal intensity at 850 nm from PA signal intensities at 680 nm and 760 nm, respectively. For each probe, two sets of three mice were conducted to confirm the reproducibility.

Acknowledgments

This work was supported by JSPS KAKENHI Grant Numbers 18H04404, 20H02811, and 21H00424. K.M. appreciates the financial supports from Hoansha Foundation, The Asahi Glass Foundation, Ogasawara Toshiaki Memorial Foundation, Iketani Science and Technology Foundation, and the “Ishizue” project in Kyoto

University. We acknowledged Prof. Teruyuki Kondo and Associate Prof. Yu Kimura in Kyoto University for PA imaging and TEM measurement. A part of this study was conducted through the Joint Usage Program of the Radiation Biology Center, Kyoto University.

Associated Content

Supporting Information

The Supporting Information is available free of charge at https://pubs.acs.org/doi/10.1021/acs.bioconjchem.0000000.

Synthesis of peptide linker, characterization and evaluation of MNc conjugates, Figures S1–S12, Tables S1–S5, and ^{1}H NMR spectra

References

1 Maturi, M., Locatelli, E., Monaco, I., and Franchini, M. C. (2019) Current concepts in nanostructured contrast media development for *in vivo* photoacoustic imaging. *Biomater. Sci. 7*, 1746–1775.

2 Weber, J., Beard, P., and Bohndiek, S. E. (2015) Contrast agents for molecular photoacoustic imaging. *Nat. Methods 13*, 639–650.

3 Wang, L. V. and Hu, S. (2013) Photoacoustic Tomography: In Vivo Imaging from Organelles to Organs. *Science 335*, 1458–1462.

4 Wang, S. and Zhang, X. (2021) Design Strategies of Photoacoustic Molecular Probes. *ChemBioChem 22*, 308–316.

5 Gujrati, V., Mishra, A., and Ntziachristos, V. (2017) Molecular imaging probes for multi-spectral optoacoustic tomography. *Chem. Commun*. *53*, 4653–4672.

6 Cheng, H.-B., Li, Y., Tang, B. Z., and Yoon, J. (2020) Assembly strategies of organic-based imaging agents for fluorescence and photoacoustic bioimaging applications. *Chem. Soc. Rev*. *49*, 21–31.

7 Ji, C., Cheng, W., Yuan, Q., Müllen, K., and Yin, M. (2019) From Dyestuff Chemistry to Cancer Theranostics: The Rise of Rylenecarboximides. *Acc. Chem. Res. 52*, 2266–2277.

8 Wang, X., Geng, Z., Cong, H., Shen, Y., and Yu, B. (2019) Organic Semiconductors for Photothermal Therapy and Photoacoustic Imaging. *ChemBioChem 20*, 1628–1636.

9 Li, J., Rao, J., and Pu, K. (2018) Recent progress on semiconducting polymer nanoparticles for molecular imaging and cancer therapy. *Biomaterials 155*, 217–235.

10 Cheng, P. and Pu, K. (2020) Activatable Phototheranostic Materials for Imaging-Guided Cancer Therapy. *ACS Appl. Mater. Inter. 12*, 5286–5299.

11 Knox, H. J. and Chan, J. (2018) Acoustogenic Probes: A New Frontier in Photoacoustic Imaging. *Acc. Chem. Res*. *51*, 2897–2905.

12 Q. Miao, K. Pu, (2016) Emerging Designs of Activatable Photoacoustic Probes for Molecular Imaging. *Bioconjugate Chem*. **27**, 2808–2823.

13 Lu, H. D., Lim, T. L., Javitt, S., Heinmiller, A., and Prud'homme, R. K. (2017) Assembly of Macrocycle

Dye Derivatives into Particles for Fluorescence and Photoacoustic Applications. *ACS Comb. Sci. 19*, 397–406.

14 Zhang, Y., Jeon, M., Rich, L. J., Hong, H., Geng, J., Zhang, Y., Shi, S., Barnhart, T. E., Alexandridis, P., Huizinga, J. D., et al. (2014) Non-invasive multimodal functional imaging of the intenstine with frozen micellar naphthalocyanine. *Nat. Nanotech. 9*, 631–638.

15 Zheng, B.-D., He, Q.-X., Li, X., Yoon, J., and Huang, J.-D. (2021) Phthalocyanines as contrast agents for photothermal therapy. *Coord. Chem. Rev*. *426*, 213648.

16 Li, X., Zheng, B.-D., Peng, X.-H., Li, S.-Z., Ying, J.-W., Zhao, Y., Huang, J.-D., and Yoon, J. (2019) Phthalocyanines as medical photosensitizers: Developments in the last five years. *Coord. Chem. Rev*. *379*, 147–160.

17 Huang, H., Wang, D., Zhang, Y., Zhou, Y., Geng, J., Chitgupi, U., Cook, T. R., Xia, J., and Lovell, J. F. (2016) Axial PEGylation of Tin Octabutoxy Naphthalocyanine Extends Blood Circulation for Photoacoustic Vascular Imaging. *Bioconjugate Chem. 27*, 1574–1578.

18 Miki, K., Inoue, T., Kobayashi, Y., Nakano, K., Matsuoka, H., Yamauchi, F., Yano, T., and Ohe, K. (2015) Near-Infrared Dye-Conjugated Amphiphilic Hyaluronic Acid Derivatives as a Dual Contrast Agent for In Vivo Optical and Photoacoustic Tumor Imaging. *Biomacromolecules 16*, 219–227.

19 Miki, K., Enomoto, A., Inout, T., Nabeshima, T., Saino, S., Shimizu, S., Matsuoka, H., and Ohe, K., (2017) Polymeric Self-Assemblies with Boron-Containing Near-Infrared Dye Dimers for Photoacoustic Imaging Probes. *Biomacromolecules 18*, 249–256.

20 Choi, M. T. M., Li, P. P. S., and Ng, D. K. P. (2000) A Direct Comparison of the Aggregation Behavior of Phthalocyanines and 2,3-Naphthalocyanines. *Tetrahedron 56*, 3881–3887.

21 Tai, S. and Hayashi, N. (1991) Strong Aggregation Properties of Novel Naphthalocyanines. *J. Chem. Soc. Perkin Trans. 2* 1275–1279.

22 Yang, Y. and Rosenberg, G. A. (2015) Matrix metalloproteinase as therapeutic targets for stroke. *Brain Res. 1623*, 30–38.

23 Fields, G. B. (2019) Mechanism of Action of Novel Drugs Targeting Angiogenesis-Promoting Matrix

Metalloproteinases. *Front. Immunol. 10*, 1278.

24 Brinckerhoff, C. E. and Matrisian, L. M. (2002) Matrix metalloproteinases: a tail of a frog that became a prince. *Nat. Rev. Mol. Cell Biol. 3*, 207–214.

25 Yin, L., Sun, H., Zhang, H., He, L., Qiu, L., Lin, J., Xia, H., Zhang, Y., Ji, S., Shi, H., et al. (2019) Quantitatively Visualising Tumor-Related Protease Activity *in Vivo* Using a Ratiometric Photoacoustic Probe. *J. Am. Chem. Soc. 141*, 3265–3273.

26 Peng, J., Yang, Q., Xiao, Y., Shi, K., Liu, Q., Hao, Y., Yang, F., Han, R., and Qian, Z. (2019) Tumor Microenvironment Responsive Drug-Dye-Peptide Nanoassembly for Enhanced Tumor-Targeting, Penetration, and Photo-Chemo-Immunotherapy. *Adv. Funct. Mater. 29*, 190004.

27 Levi, J., Kothapalli, S.-R., Bohndiek, S., Yoon, J.-K., Dragulescu-Andrasi, A., Nielsen, C., Tisma, A., Bodapati, S., Goweishankar, G., Yan, X., et al. (2013) Molecular Photoacoustic Imaging of Follicular Thyroid Carcinoma. *Clin. Cancer Res. 19*, 1494–1502.

28 Levi, J., Kothapalli, S. R., Ma, T.-J., Hartman, K., Khuri-Yakub, B. T., and Gambhir, S. S. (2010) Design, Synthesis, and Imaging of an Activatable Photoacoustic Probe. *J. Am. Chem. Soc. 132*, 11264–11269.

29 Ford, W. E., Rodgers, M. A. J., Schechtman, L. A., Sounik, J. R., Rihter, B. D., and Kenney, M. E. (1992) Synthesis and Photochemical Properties of Aluminum, Gallium, Silicon, and Tin Naphthalocyanines. *Inorg. Chem. 31*, 3371–3377.

30 Sato, K., Ando, K., Okuyama, S., Mariguchi, S., Ogura, T., Totoki, S., Hanaoka, H., Nagaya, T., Kokawa, R., Takakura, H., et al. (2018) Photoinduced Ligand Release from a Silicon Phthalocyanine Dye Conjugated with Monoclonal Antibodies: A Mechanism of Cancer Cell Cytotoxicity after Near-Infrared Photoimmunotherapy. *ACS Cent. Sci. 4*, 1559–1569.

31 Song, K.-H., Gu, M., Kim, M.-S., Kwon, H.-J., Rhee, H., Han, H., and Cho, M. (2015) Quantum Beats and Phase Shifts in Two-Dimensional Electronic Spectra of Zinc Naphthalocyanine Monomer and Aggregate. *J. Phys. Chem. Lett. 6*, 4314–4318.

32 Luan, L., Chen, J., Ding, L., Wang, J., Cheng, X., Ren, Q., and Liu, W. (2012) Tetrabrominated Naphthalocyaninatozinc Complex with Terminal Carboxylate Functionalities. *Chem. Lett. 41*, 1012–1014.

33 Ito, F., Inoue, T., Tomita, D., and Nagamura, T. (2009) Excited-State Relaxation Process of Free-Base and Oxovanadium Naphthalocyanine in Near-Infrared Region. *J. Phys. Chem. B 113*, 5458–5463.

34 Wang, H., Li, X., Tse, B. W.-C., Yang, H., Thorling, C. A., Liu, Y., Touraud, M., Chouane, J. B., Liu, X., Roberts, M. S., et al. (2018) Indocyanine green-incorporating nanoparticles for cancer theranostics. *Theranostics 8*, 1227–1242.

35 Schaafsma, B. E., Mieog, J. S. D., Hutteman, M., van der Vorst, J. R., Kuppen, P. J. K., Löwik, C. W. G. M., Frangioni, J. V., van de Velde, C. J. H., and Vahrmeijer, A. L. (2011) The Clinical Use of Indocyanine Green as a Near-Infrared Fluorescent Contrast Agent for Image-Guided Oncologic Surgery. *J. Surg. Oncol*. *104*, 323–332.

36 Prado, A. F., Pernomian, L., Azevedo, A., Costa, R. A. P., Rizzi, E., Ramos, J., Paes Leme, A. F., Bendhack, L. M., and Tanus-Santos, J. E. (2018) Matrix metalloproteinase-2-induced epidermal growth factor receptor transactivation impairs redox balance in vascular smooth muscle cells and facilitates vascular contraction. *Redox Biol. 18*, 181–190.

37 Akers, W. J., Xu, B., Lee, H., Sudlow, G. P., Fields, G. B., Achilefu, S., Edwards, W. B. (2012) Detection of MMP-2 and MMP-9 Activity *in Vivo* with a triple-Helical Peptide Optical Probe. *Bioconjugate Chem. 23*, 656–663.

38 Zhang, X., Bresee, J., Fields, G. B., Edwards, W. B. (2014) Near-infrared triple-helical peptide with quenched fluorophores for optical imaging of MMP-2 and MMP-9 proteolytic activity in vivo. *Bioorg. Med. Chem. Lett*. *24*, 3786–3790.

39 Wu, Y., Wang, A., Ding, X., Xu, F.-J. (2017) Versatile Functionalization of Poly(methacrylic acid) Brushes with Series of Proteolytically Cleavable Peptides for Highly Sensitive Protease Assay. *ACS Appl. Mater. Inter*. *9*, 127–135.

40 Giambernardi, T. A., Grant, G. M., Taylor, G. P., Hay, R. J., Maher, V. M., McCormick, J. J., Klebe, R. J. (1998) Overview of Matrix Metalloproteinase Expression in Cultured Human Cells. *Matrix Biol*. *16*, 483–496.

41 Matsumura, Y., Maeda, H. (1986) A New Concept of Macromolecular Therapeutics in Cancer

Chemotherapy: Mechanism of Tumoritropic Accumulation of Proteins and the Antitumor Agent Smancs. *Cancer. Res*. *46*, 6387–6392.

42 Huang, H., Yue, T., Xu, Y., Xu, K., Xu, H., Liu, S., Yu, J., and Huang, J. (2015) PEGylation of MnO nanoparticles via catechol-Mn chelation to improving T_1-weighted magnetic resonance imaging application. *J. Appl. Polym. Sci*. *132*, 42360.

TOC

width x height: 3.5 inch x 2 inch (9 cm x 5.1 cm)